

# Fast Photoresponse from Hybrid Monolayer MoS<sub>2</sub>/Organic Photodetector

Meysam Raoufi, Steffen Rühl, Sreelakshmi Chandrabose, Atul Shukla, Bowen Sun, Emil-List Kratochvil, Sylke Blumstengel, and Dieter Neher\*

As a direct-bandgap transition semiconductor with high carrier mobility, monolayer (ML) transition metal dichalcogenides (TMDCs) have attracted significant attention as a promising class of material for photodetection. It is reported that these layers exhibit a persistent photoconductance (PPC) effect, which is assigned to long-lasting hole capture by deep traps. Therefore, TMDCs-based photodetectors show a high photoresponse but also a slow response. Herein, intensity-modulated photocurrent spectroscopy (IMPS) with steady-state background illumination is performed to investigate the photoresponse dynamics in a hybrid photodetector based on ML MoS<sub>2</sub> covered with an ultrathin layer of phthalocyanine (H<sub>2</sub>Pc) molecules. The results demonstrate that adding the H<sub>2</sub>Pc layer speeds up the photoresponse of the neat ML-MoS<sub>2</sub> photodetector by almost two orders of magnitude without deteriorating its responsivity. The origin of these improvements is revealed by applying the Hornbeck–Haynes model to the photocarrier dynamics in the IMPS experiment. It is shown that the improved response speed of the hybrid device arises mostly from a faster detrapping of holes in the presence of the H<sub>2</sub>Pc layer, while the trap densities remain rather unchanged. Meanwhile, the additional absorption of photons in the H<sub>2</sub>Pc layer contributes to photocarrier generation, resulting in an enlarged responsivity of the hybrid device.

## 1. Introduction

Monolayer (ML) transition metal dichalcogenides (TMDCs) are being intensively investigated due to their excellent physical and chemical properties. Among TMDCs, molybdenum disulfide (MoS<sub>2</sub>) possesses a relatively high carrier mobility<sup>[1]</sup> and strong light absorption, offering great potential for optoelectronic applications such as sensitive and broadband photodetectors.<sup>[2–6]</sup> Several reports have shown that ML-MoS<sub>2</sub> exhibits persistent photoconductance (PPC).<sup>[7–10]</sup> PPC is a light-induced conductivity that lasts for longer durations after photoexcitation, sometimes even for days. As the free carrier recombination in ML-MoS<sub>2</sub> is fast, usually at the subnanosecond scale, the origin of PPC is attributed to trapping of one of the carriers, therefore increasing the effective lifetime of the opposite charge. The origin of these traps has often been assigned to extrinsic reasons including carrier trapping by the substrate<sup>[11]</sup> and on adsorbates.<sup>[12–14]</sup>


In contrast, Turchanin and co-workers reported that extrinsic factors may play a minor role and attributed carrier trapping to intrinsic localized states in the forbidden gap arising from defect sites.<sup>[7]</sup> They further concluded that crystal lattice defects and lattice strain lead to large spatial fluctuations of the potential energy of carriers. These fluctuations introduce a spatial separation of photogenerated carriers where electrons (holes) accumulate in the minima (maxima) of the potential energy landscape, resulting in the prolongation of their recombination time. Irrespective of the reasons, this process can significantly improve the photosensitivity of the detector but also limit the response speed of the device. Various approaches of defect engineering have been used in ML MoS<sub>2</sub> to enhance the dynamic response; however, most of these approaches lead to a strong reduction in photosensitivity due to the elimination of the trap-induced gain mechanism.<sup>[15]</sup>

Several studies combined ML-TMDCs with organic semiconductors in hybrid Van der Waals heterostructures to improve the performance of the photodetectors. Zhenhua Ni and co-workers demonstrated improved response time and responsivity of the ReS<sub>2</sub>-based detector via molecular decoration with an organic chromophore, protoporphyrin. The protoporphyrin layer was proposed to passivate deep traps, allowing the device response speed to be dominated only by carrier recombination and shallow

M. Raoufi, S. Chandrabose, A. Shukla, B. Sun, D. Neher  
 Institute of Physics and Astronomy  
 University of Potsdam  
 14476 Potsdam, Germany  
 E-mail: neher@uni-potsdam.de

S. Rühl, E.-L. Kratochvil, S. Blumstengel  
 Institut für Chemie  
 Institut für Physik und IRIS Adlershof  
 Humboldt-Universität zu Berlin  
 Zum Großen Windkanal 2, 12489 Berlin, Germany

E.-L. Kratochvil  
 Helmholtz-Zentrum Berlin für Materialien und Energie  
 Hahn-Meitner-Platz 1, 14109 Berlin, Germany

 The ORCID identification number(s) for the author(s) of this article can be found under <https://doi.org/10.1002/pssa.202300107>.

© 2023 The Authors. physica status solidi (a) applications and materials science published by Wiley-VCH GmbH. This is an open access article under the terms of the Creative Commons Attribution License, which permits use, distribution and reproduction in any medium, provided the original work is properly cited.

DOI: 10.1002/pssa.202300107

traps.<sup>[16]</sup> In a similar work, Lee et.al reported a shorter decay time of a hybrid ML-MoS<sub>2</sub>/copper (II) phthalocyanine (CuPc) detector in comparison to that of pristine ML-MoS<sub>2</sub>. They deduced that the thin layer of CuPc prevents adsorption of oxygen on the surface of MoS<sub>2</sub> layer, which induces faster response times. Also, the higher responsivity of the hybrid heterostructure was attributed to interfacial photogenerated charge transfer.<sup>[17,18]</sup> Apart from CuPc and protoporphyrin, zinc phthalocyanine (ZnPc) on ML MoS<sub>2</sub> has also been demonstrated to introduce an interfacial charge transfer channel, which suppresses the slow minority carrier trapping to the inherent trap states in MoS<sub>2</sub> and the substrates, resulting in an accelerated response speed.<sup>[19]</sup> They achieved simultaneous improvement in photoresponsivity and response time by combining dielectric passivation and a gate modulation method.<sup>[19]</sup> For a brief overview of the compared characteristics of the aforementioned devices, please refer to Table S1, Supporting Information.

Related to this, an important question is how the addition of organic semiconductors affects crucial properties such as the trap density and the trapping–detrapping dynamics. A popular approach to explain the PPC in neat TMDCs and hybrid heterostructures is the Hornbeck–Haynes model. Here, electrons are assumed to be the mobile carriers (dominating the photocurrent) while holes become localized on traps which are not accessible to electrons. As a consequence of trap filling, the photosensitivity and the response time are predicted to depend on the illumination intensity in a characteristic way. This has been used in the past to gain information on the trap density and the rates for trapping, detrapping, and recombination. To access these parameters, it is common to measure the rise and decay of the photocurrent upon illumination with a rectangular intensity profile, where the intensity in the on-state is systematically increased. This “large-signal” approach has, however, the disadvantage that the trap occupation, which determines the device response, changes itself during the signal rise and decay.<sup>[20]</sup>

In this work, we use a different approach, namely, intensity-modulated photocurrent spectroscopy (IMPS) in combination with steady-state background (BG) illumination. By applying the Hornbeck–Haynes model to this illumination scheme, we show that the detrapping rate can be separately determined from the other kinetic parameters. We apply this approach to neat ML-MoS<sub>2</sub> and a bilayer with a 3 nm-layer thickness of the hydrogenated phthalocyanine (H<sub>2</sub>Pc). Using a lateral two-point device architecture instead of a transistor, we avoid contributions from photogating.<sup>[21]</sup> We show that the presence of H<sub>2</sub>Pc layer on MoS<sub>2</sub> simultaneously improves the photoresponsivity and response speed of detector. As such, the hybrid device exhibits improved sensitivity at higher frequency and over a wider spectral range. Interestingly, the detailed analysis of the IMPS as a function of frequency and BG illumination intensity reveals similar trap densities for the neat MoS<sub>2</sub> and hybrid samples, ruling out trap passivation as the reason for the faster response of the bilayer device. Instead, we identify faster detrapping of holes in the presence of the organic layer as the dominant reason for improved response speed. Our results provide vital information for the future development of TMDC/organic heterojunction-based photodetectors.

## 2. Results

### 2.1. Device Layout and Basic Optoelectronic Properties

We fabricated photodetectors with bare ML-MoS<sub>2</sub> and a hybrid structure with the ML-MoS<sub>2</sub> coated by a 3 nm-thin layer of H<sub>2</sub>Pc. The H<sub>2</sub>Pc molecule was chosen specifically due to its high chemical stability. Furthermore, according to the reported energy diagram,<sup>[21]</sup> shown in **Figure 1a**, there is proper energy offset between the occupied and the unoccupied levels and as a consequence sufficient driving force for exciton dissociation and interfacial charge transfer. A previous study of steady-state

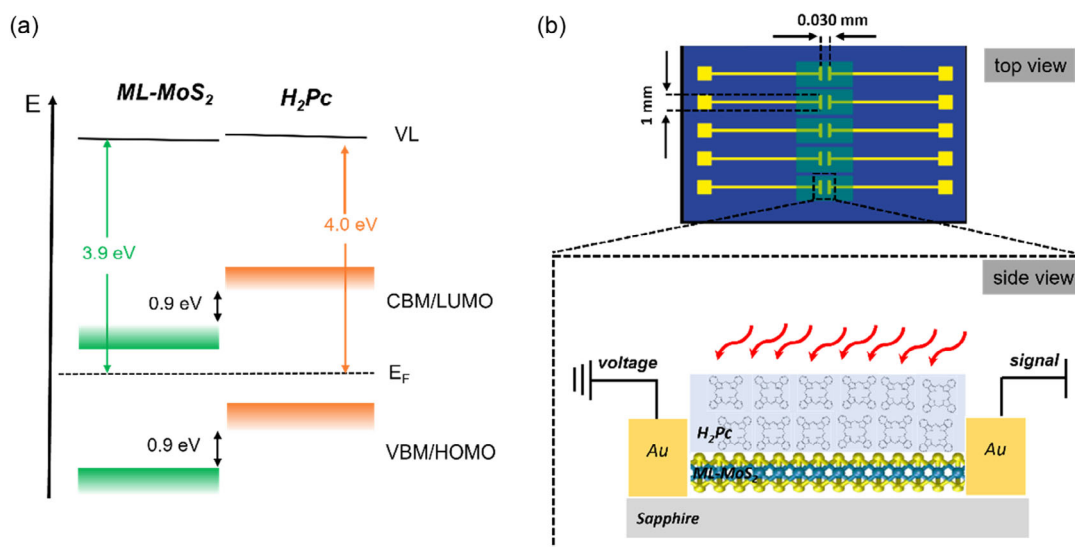


**Figure 1.** a) Energy-level diagram of the MoS<sub>2</sub>/H<sub>2</sub>Pc interface and b) scheme (top and side view) of the ML-MoS<sub>2</sub>/H<sub>2</sub>Pc van der Waals heterojunction photodetector with a 3 nm H<sub>2</sub>Pc layer. The ML-MoS<sub>2</sub> is composed of molybdenum atoms (blue spheres) which are sandwiched between two layers of sulfur atoms (gold spheres).

photoluminescence (PL) spectroscopy demonstrated efficient exciton dissociation across this hybrid interface.<sup>[22,23]</sup> In addition, ultrafast charge transfer between ML-MoS<sub>2</sub> and H<sub>2</sub>Pc, monitored via the transient absorption spectroscopy technique, has been reported.<sup>[24,25]</sup>

The sample design for the heterojunction-based photodetector is schematically illustrated in Figure 1b. The active area between two electrical contacts (Au) is around 0.03 mm<sup>2</sup>. As pointed out in the introduction, we prefer the two-point lateral device over a phototransistor because photogating is absent.<sup>[21]</sup>

**Figure 2a** shows the incident photon to collected electron conversion efficiency (IPCE) spectra of the neat MoS<sub>2</sub> and the hybrid device, measured at 10 Hz. All IPCE measurements were done on the same ML-MoS<sub>2</sub> before and after H<sub>2</sub>Pc layer deposition. The absolute IPCE value was calculated from measured modulated current of the devices and a Si detector as a reference. The IPCE spectrum of the ML-MoS<sub>2</sub> device follows the absorption spectrum, with the characteristic excitonic transitions of A-exciton and B-exciton at 607 and 654 nm, respectively. The IPCE spectrum of the hybrid displays the same features superimposed by a broad absorption which we assign to H<sub>2</sub>Pc (see Figure 2b for the spectrum of H<sub>2</sub>Pc on quartz). For further analysis, we subtracted the bare ML-MoS<sub>2</sub> absorption spectrum from the heterostructure spectrum to obtain the spectrum of the H<sub>2</sub>Pc on the actual ML-MoS<sub>2</sub>, see Figure 2c. The spectral difference compared to the spectrum in Figure 2b can be attributed to different packing of H<sub>2</sub>Pc on the ML-MoS<sub>2</sub>.<sup>[22]</sup> To provide a more detailed explanation, we performed a quantitative analysis to determine the individual contributions of the neat ML-MoS<sub>2</sub> and H<sub>2</sub>Pc to the IPCE spectrum. This involved reconstructing the IPCE by superimposing the absorption spectra of the neat ML-MoS<sub>2</sub> and H<sub>2</sub>Pc (on MoS<sub>2</sub>). This reconstruction is shown with a black line in Figure 2d. According to our analysis, the H<sub>2</sub>Pc layer (which makes up 57% of the hybrid device) has a greater impact

on photogeneration than the ML-MoS<sub>2</sub> layer (which makes up 43%). This is because the H<sub>2</sub>Pc layer has a stronger and broader absorption spectrum compared to the ML-MoS<sub>2</sub> layer. Our findings indicate that the increased absorption provided by the organic layer is the main reason for the higher IPCE in the hybrid device.

Importantly, the IPCE of the ML-MoS<sub>2</sub> approaches unity while the heterostructure-based device even exhibits this value. This is a clear feature of photoconductivity gain. We assume in the following that electrons dominate the photocurrent. In the ideal case, every electron leaving the layer through one of the electrodes is replenished by an electron from the other electrode. Then, the electron density in the sample is determined by the dynamic generation–recombination equilibrium:  $G = R = -\frac{dn}{dt} = \Delta n/\tau_e$  or  $\Delta n = \tau_e G$ . Here,  $G$  and  $R$  is the charge generation and recombination rate, respectively,  $\Delta n$  is the photogenerated excess electron density, and  $\tau_e$  the free electron lifetime. The IPCE can then be related to the external quantum efficiency of photogeneration  $\eta_{\text{ext}}$  and the free carrier mobility,  $\mu_e$  via

$$\text{IPCE} = \eta_{\text{ext}} \frac{\mu_e \tau_e E}{L} = \eta_{\text{ext}} \frac{L_{\text{drift}}}{L} \quad (1)$$

where  $E$  is the electric field,  $L$  is the length of the active channel, and  $L_{\text{drift}} = \mu_e \tau_e E$  is the drift length (for more details, see Note S1, Supporting Information). According to this equation, photoconductivity gain is observed when  $L_{\text{drift}}$  exceeds  $L$ , which for the given channel length and under realistic conditions is only possible if  $\tau_e$  is of the order of milliseconds or more. A prediction of Equation (1) is that the photoconductivity gain and with this IPCE is proportional to the applied voltage. This is indeed the case for our samples, as shown in Figure S1, Supporting Information. Notably, the shape of the ICPE spectrum is not affected by the applied voltage. This means that the very same

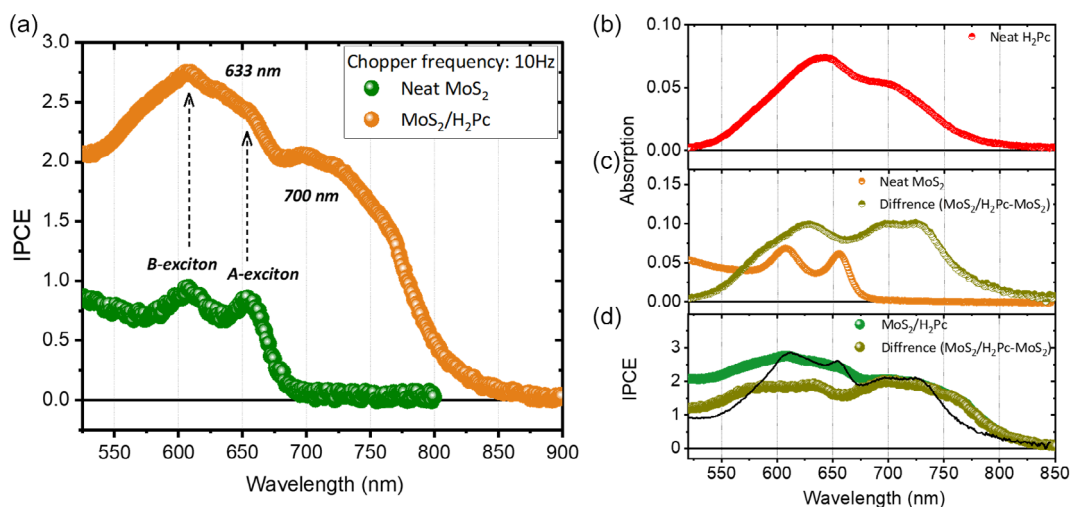


**Figure 2.** a) IPCE spectrum of a neat ML-MoS<sub>2</sub> and a ML-MoS<sub>2</sub>/H<sub>2</sub>Pc hybrid device. Measurements were performed under N<sub>2</sub> atmosphere and devices were illuminated only with chopped light. The arrows show the corresponding positions of the MoS<sub>2</sub> A- and B-exciton. b, c) Absorption spectra of neat H<sub>2</sub>Pc on quartz and of the neat ML-MoS<sub>2</sub>. Also shown is the difference of the absorption of the heterostructure and the neat ML-MoS<sub>2</sub> sample, which is a good approximation of the absorption of H<sub>2</sub>Pc on the ML-MoS<sub>2</sub>. d) IPCE spectrum of hybrid device and difference in IPCE of the hybrid device and the ML-MoS<sub>2</sub>. The black line along to IPCE spectra of hybrid device is the superposition of the absorption of the neat ML-MoS<sub>2</sub> and of the H<sub>2</sub>Pc (on MoS<sub>2</sub>) from ©.

mechanism causes the gain irrespectively whether MoS<sub>2</sub> or H<sub>2</sub>Pc is primarily excited. We also note that the measured dark current–voltage curve (see Figure S2, Supporting Information) of the hybrid and ML-MoS<sub>2</sub> devices display ohmic behavior, indicating the absence of charge injection barriers.

## 2.2. Intensity-Modulated Photocurrent Spectroscopy (IMPS)

We combine frequency-dependent measurement along with steady-state BG illumination, as depicted in **Figure 3a**, in order to analyze the mechanism behind the PPC for both devices.

Figure 3b presents the absolute IPCE of both devices, measured without any BG illumination, as a function of modulation frequency (1 Hz–1 KHz). The excitation wavelengths were  $\lambda_{\text{ex}} = 650$  nm and  $\lambda_{\text{ex}} = 630$  nm for the neat ML-MoS<sub>2</sub> and hybrid devices, respectively. Both devices show a roll-off of the IPCE value at high modulation frequencies, which is however significantly reduced for the hybrid device. Combined with the larger absorption, the hybrid device displays a higher photoconductive gain over the entire frequency spectrum. Figure 3c shows the IPCE of both devices, measured at a frequency of 120 Hz as a

function of the BG photon flux density ( $\Phi_{\text{BG}}$ ). For both devices, the IPCE approaches a constant value for low intensities but decreases inversely proportional to  $\Phi_{\text{BG}}$  for the high intensities. The latter phenomena are usually attributed to hole trapping, where BG illumination fills these traps and accordingly reduces the density of traps available for the persistent photoconductivity.<sup>[19,26]</sup>

To analyze the photoconductive response dynamics quantitatively, we adapted the Hornbeck–Haynes model which is schematically illustrated in Figure 3d. Here, hole trapping is via a distribution of traps above the valance band ( $E_v$ ), with the density  $N_t$ . Electron trapping is neglected in this model considering the *n*-doped nature of ML-MoS<sub>2</sub> in which the Fermi level ( $E_F$ ) is close to the conduction band ( $E_c$ ) edge and, therefore, most of the electron traps are filled.<sup>[27]</sup> The hole trapping and detrapping lifetimes are described by  $\tau_t$  and  $\tau_d$ , respectively. Further,  $\tau_r$  describes the recombination of electron and hole through midgap states (Shockley–Read–Hall recombination).<sup>[28]</sup> Assuming charge neutrality and strong *n*-doping, the photoinduced excess electron density is equal to the sum of the free and trapped hole density,  $p$  and  $\rho$ , respectively:  $\Delta n(t) = p(t) + \rho(t)$ . We then apply

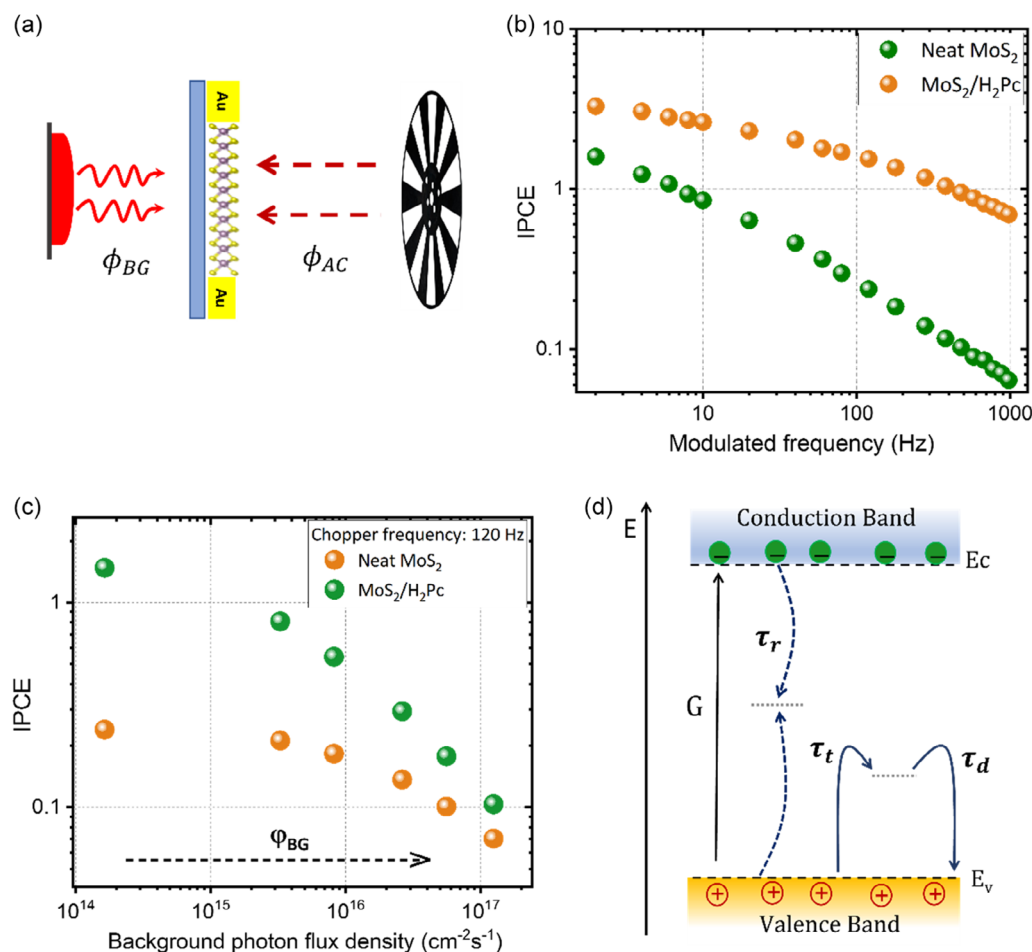


**Figure 3.** a) Schematic of the experimental setup with both modulated and steady-state background light. b) IPCE of the device with neat ML-MoS<sub>2</sub> ( $\lambda_{\text{ex}} = 650$  nm) and hybrid device ( $\lambda_{\text{ex}} = 630$  nm) as a function of modulation frequency. c) Impact of steady-state BG illumination on the IPCE value of neat ML-MoS<sub>2</sub> and hybrid device. d) Simplified energy band diagram and possible processes contributing to the photoconductivity mechanism including generation (*G*), midgap recombination ( $\tau_r$ ), trapping ( $\tau_t$ ), and release ( $\tau_d$ ).



a time-dependent charge generation rate,  $G(t) = G_0 + G_1 e^{i\omega t}$  to the Hornbeck–Haynes model to yield the zero-frequency and first-harmonic components of the time-dependent trapped hole density,  $\rho = \rho_0 + \rho_1 e^{i\omega t}$ . Further assuming, that  $p(t) \ll \rho(t)$ , one obtains the following equations for the steady-state and first-harmonic electron excess electron densities.

$$\Delta n_0 \cong \rho_0 = \tau_q G_0 \quad (2)$$

and

$$\Delta n_1(\omega) \cong \rho_1(\omega) = \frac{\tau_q}{1 + i\omega\tau} G_1 \quad (3)$$

This is detailed in Note S2, Supporting Information. Evidently,  $\tau_q = \frac{\tau_{q0}}{1 + \tau_{q0} \frac{G_0}{N_t}}$  in Equation 2 and 3 has the meaning of a carrier (electron) lifetime, which for zero-background generation rate ( $G_0 \rightarrow 0$ ) becomes  $\tau_{q0} = \frac{\kappa_1}{\kappa_r \kappa_d} = \tau_r \frac{\tau_d}{\tau_i}$ . The second important property is  $\tau = \frac{\tau_{q0} + \tau_d}{1 + \tau_{q0} \frac{G_0}{N_t}}$  which is the response time of the device.

There are two important predictions of these equations. First, the first-harmonic component of the trapped hole density (and with that of the excess electron density and the photoconductivity) has a Debye-type dependence on the modulation frequency.

This allows us to extract the values of  $\tau_q$  and  $\tau$  as a function of  $G_0$ . Second,  $\tau_q$  and  $\tau$  have the same dependence on  $G_0$  but they differ in their absolute values. The reason is that both times stand for two significantly different processes (see Note S3, Supporting Information).  $\tau_q$  describes the steady-state situation and it is the ratio of the steady-state excess electron density and the electron generation rate under BG illumination. In contrast,  $\tau$  describes how the device reacts to changes in the illumination conditions. We will show in the following that  $\tau_q$  and  $\tau$  are indeed rather different for the two samples.

Figure 4a shows the in-phase (X) and out-of-phase (Y) components of the IMPS response, measured between 1 Hz and 1 KHz in the absence of BG illumination. In these measurements, the response is shown plotted in arbitrary units as the photocurrent was not calibrated against a Si reference. For the neat ML-MoS<sub>2</sub> device, the in-phase component does not level off at low frequency in contrast to the hybrid device, which is indicative of slower response dynamics in the bare ML-MoS<sub>2</sub>. According to Equation (3), the frequency dependence of the IMPS should follow a simply Debye relaxation behavior. However, reasonable fits to the spectra were only obtained by adopting the simplified Havriliak–Negami (HN) equation,<sup>[29,30]</sup> an empirical modification of the Debye model which considers a distribution of response frequencies.

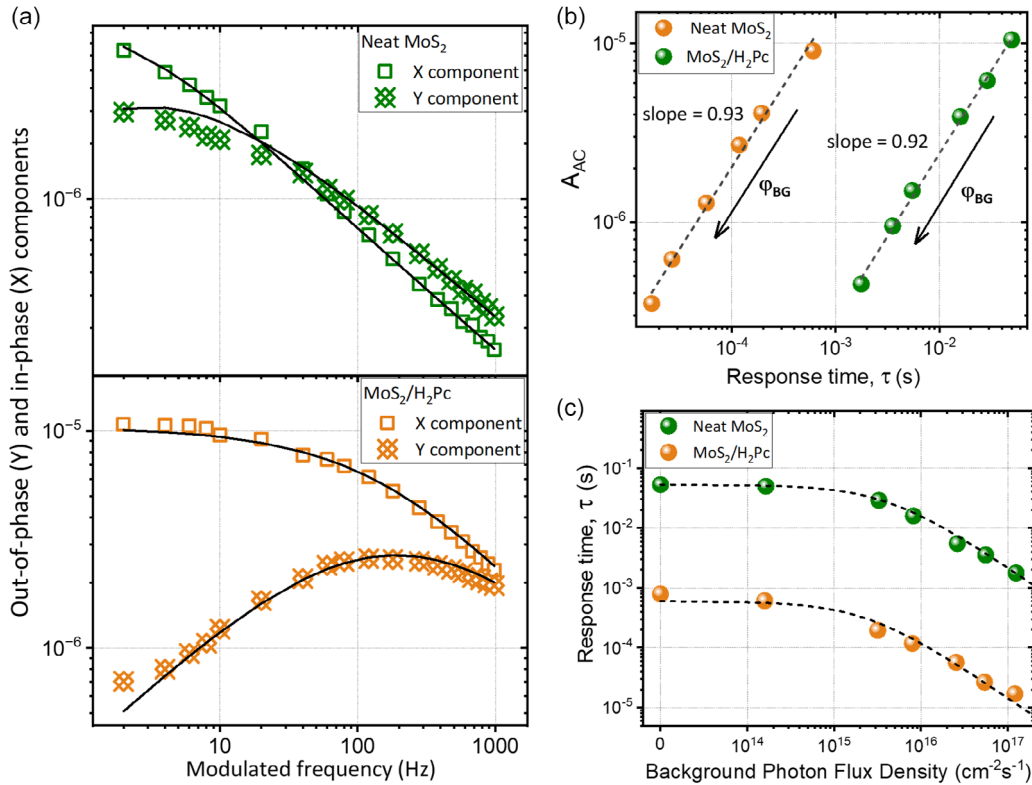


**Figure 4.** a) In-phase (X) and out-of-phase (Y) components of IMPS spectra of the neat ML-MoS<sub>2</sub> sample and the hybrid device versus the modulation frequency. b) Steady-state device response ( $A_{AC}$ ), extracted from the data in Figure S3 and S4, Supporting Information, with Equation (4), plotted as a function of the response time. The arrows presenting the effect of increasing the BG illumination on device response and response dynamics. c) Device response time ( $\tau$ ) as a function of BG illumination intensity. Dashed lines are fits to  $\tau = \frac{\tau_{q0} + \tau_d}{1 + \tau_{q0} \frac{G_0}{N_t}}$ .

$$R_{AC}(\omega) = \frac{A_{AC}}{1 + (i\omega\tau)^\alpha} \quad (4)$$

Here,  $R_{AC} \propto \Delta n_1 \cong \rho_1$  is the frequency-dependent IMPS response,  $A_{AC}(R_{AC}(\omega \rightarrow 0))$  is the steady-state response at zero-frequency modulation,  $\tau$  is the device response time as defined above, and  $\alpha$  is a parameter ranging from 0 to 1, describing the broadness of the spectra.<sup>[29]</sup> The black solid curves in Figure 4a show the best fits to Equation (4), which very well reproduce the spectra except of the Y-components at the smallest frequencies. The extracted device response time is 790  $\mu$ s and 53 ms for the hybrid and neat MoS<sub>2</sub> devices, respectively. Apparently, the presence of the organic layer leads to a significant shortening of the photoresponse dynamics of the device, as reported by others.

Figure S3 and S4, Supporting Information, show the frequency-dependent IMPS spectra of the two samples for different BG illumination intensities. The black solid curves show the best fits to Equation (4). By increasing the BG light intensity, the response time of both devices decreases, and the steady-state detector responsivity reduces. According to Equation (3), the steady-state device response ( $A_{AC}$ ) is proportional to  $\tau_q$ , which bears the same dependence on the background charge generation efficiency as the device response ( $\tau$ ). Indeed, both decrease in the same way as function of  $\phi_{BG}$  (Figure 4b), as a consequence of reducing the density of available sites for hole trapping. The dashed line highlights the linear dependence between the response time and  $A_{AC}$  as a function of BG illumination intensity or, alternatively, the linear relation between response time and free electron density upon changing BG illumination.

Figure 4c plots the response time of both devices as a function of the BG photon flux density. The device response time remains constant under low BG intensities, while it accelerates when increasing the intensity above a certain value. This dependence is in accordance with  $\tau = \frac{\tau_{q0} + \tau_d}{1 + \tau_{q0} N_t / C_0}$ . To determine  $\tau_{q0}$ , we combined the frequency-dependent IMPS response (Figure 3b) with the IPCE at 120 Hz in the absence of BG light (Figure 3a) to determine the zero-frequency steady-state IPCE. This yielded a zero-frequency steady-state IPCE of 2.6 and 3.0 for the neat ML-MoS<sub>2</sub> and the hybrid device, respectively. Then,  $\tau_{q0} \cong \tau_e$  was gained through application of Equation 1. Here, we assumed that every absorbed photon creates a charge, meaning that  $\eta_{ext}$  is equal to the absorption at the respective wavelength. Finally, an electron mobility of 1 cm<sup>2</sup> V<sup>-1</sup> s<sup>-1</sup> was used, which is typically for ML-MoS<sub>2</sub>.<sup>[7,31]</sup> The deduced values are very similar for both devices (see Table 1), despite the rather different device response. With the knowledge of  $\tau_{q0}$ , the fit of the device response time in

Figure 4c yields the trap density  $N_t$ . As for  $\tau_{q0}$ , the trap density for both devices is in the similar range. The deduced value of  $\approx 1 \times 10^{10}$  cm<sup>-2</sup> is consistent with reported data<sup>[26,32]</sup> This finding rules out trap passivation by the H<sub>2</sub>Pc layer, in agreement with recent report by Amsterdam and co-workers.<sup>[23]</sup> The main difference between the two devices lies in the value of  $\tau_d$ , determined from the zero-frequency value of  $\tau$  which is equal to  $\tau_{q0} + \tau_d$ . Here, the hybrid device shows a nearly 100 times faster detrapping.

### 3. Discussion

We have shown that the addition of H<sub>2</sub>Pc layer to ML-MoS<sub>2</sub> causes a mild increase of the IPCE but a large improvement of the response speed. Our analysis shows that the former is due to the additional absorption by the organic layer, while the carrier lifetime is essentially the same. Furthermore, we find rather similar trap densities in both systems. This suggests that the H<sub>2</sub>Pc layer neither passivates existing traps in ML-MoS<sub>2</sub> and nor does it bypass the trapping. This is in contrast to conclusions from previous works.<sup>[24,33]</sup> It has been shown that H<sub>2</sub>Pc adopts a mixed edge-on and face-on orientation, with molecular density of 10<sup>14</sup> cm<sup>-2</sup>.<sup>[24,34]</sup> If we assume that every H<sub>2</sub>Pc molecule is able to accept a hole (and act as a temporary trap), we predict a trap density of 10<sup>14</sup> cm<sup>-2</sup>. This is much larger than our measured value. Also, transient absorption spectroscopy showed that the lifetime of the charge separated state is only 4 ns, too short to cause an appreciable PPC. Instead, we propose that it's the same species that causes hole trapping in both the neat and the hybrid devices and that its intrinsic to ML-MoS<sub>2</sub> on sapphire. The main difference between the systems lies in the fact that detrapping is largely accelerated in the presence of the organic layer, being the main reason for the improvement in response speed. This improvement may be attributed to a more appropriate energy-level alignment between the highest occupied molecular orbital (HOMO) energy level of H<sub>2</sub>Pc and the deep hole trap of ML-MoS<sub>2</sub>, as schematically shown in Figure 5. Here, the same deep trap is either occupied by hole trapping from the MoS<sub>2</sub> valence band (VB) or from a photogenerated hole on the H<sub>2</sub>Pc HOMO. Clearly, the detrapping of holes will benefit from the presence of the H<sub>2</sub>Pc HOMO as an intermediate energy level.

In both scenarios, an important precondition is that the deep hole traps are not accessible to free electrons in the MoS<sub>2</sub> VB; otherwise, fast capture of these electrons by these traps is expected. A possible explanation is the model of spatially separated electrons and holes due to potential fluctuations as proposed by Turchanin and coworkers.<sup>[7]</sup> In this case, another time range would enter, namely, of the electrons to leave the energy well and become again accessible to recombine with holes. Since such potential fluctuations depend on the properties of the ML-MoS<sub>2</sub> and its interaction with the substrate, they might play a similar role in both samples and actually explain the rather similar electron lifetimes for both types of devices. The inclusion of this additional channel will, however, very much complicate the analytical model and the analysis, which is beyond the scope of this article.

**Table 1.** Steady-State charge carrier lifetime ( $\tau_{q0}$ ), detrapping time ( $\tau_d$ ), and trap density ( $N_t$ ) as deduced from the application of Equation (1) and (3) to the data in Figure 2, 4, and S4, Supporting Information.

	$\tau_{q0}$ [s]	$\tau_d$ [s]	$N_t$ [cm <sup>-2</sup> ]
ML-MoS <sub>2</sub>	$0.5 \times 10^{-4}$	$530 \times 10^{-4}$	$0.7 \times 10^{10}$
Hybrid (MoS <sub>2</sub> /H <sub>2</sub> Pc)	$0.3 \times 10^{-4}$	$7.6 \times 10^{-4}$	$0.4 \times 10^{10}$

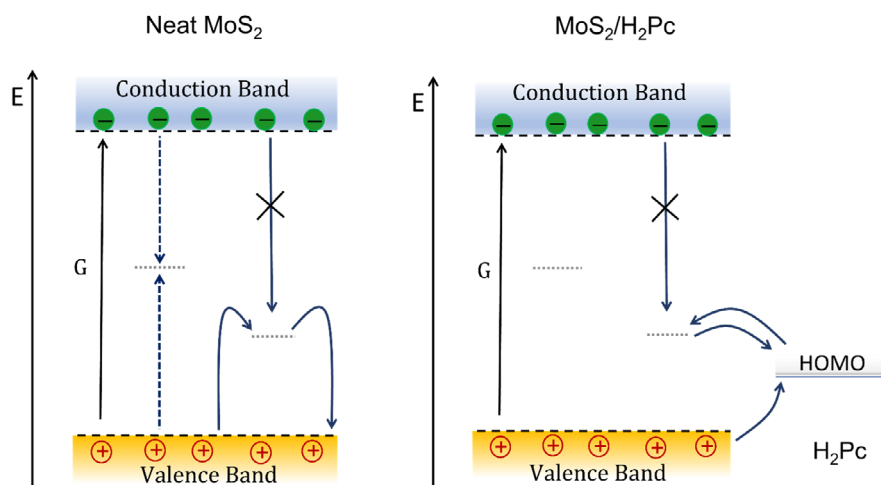


**Figure 5.** The energy band diagram of the neat ML-MoS<sub>2</sub> and hybrid (MoS<sub>2</sub>/H<sub>2</sub>Pc) samples. Arrows show the generation, trapping, transfer, and recombination of charges upon direct ML-MoS<sub>2</sub> excitation. Presuming that there is one common deep hole trap in both devices, detrapping would benefit from the presence of the organic HOMO with intermediate energy in the hybrid device.

## 4. Conclusion

In summary, we show that the presence of organic layer leads to an improvement in the response dynamics and photoresponsivity of the hybrid photodetector. The hybrid detector is found to show broadband spectral responsivity with improvement in the responsivity at high frequencies. IMPS with variable background illumination was combined with an analytical model to yield the processes behind the improved performance. Our findings reveal similar trap densities and carrier lifetimes for both systems. We further show negligible trap passivation due to the organic layer coating; instead, improved response dynamics of the hybrid system can be attributed to the enhancement in the detrapping rate.

## 5. Experimental Section

**Material and Sample Preparation:** In this study, we used exfoliated ML of MoS<sub>2</sub> (ML-MoS<sub>2</sub>) and organic molecule of phthalocyanine (H<sub>2</sub>Pc, C<sub>32</sub>H<sub>18</sub>N<sub>8</sub>) purchased from Sigma-Aldrich Inc. For the MoS<sub>2</sub> exfoliation, ultraflat template-stripped Au was used as exfoliation membrane. MoS<sub>2</sub> crystal (2D semiconductors, synthetic MoS<sub>2</sub> crystal) is cleaved with the help of Kapton tape and the freshly exposed MoS<sub>2</sub> surface was pressed onto the ultraflat gold membrane. After heating at 200 °C for 1 min, the MoS<sub>2</sub>-carrying Kapton tape could be removed, leaving MLs on gold behind. For a detailed description of the process and a full MoS<sub>2</sub> characterization, see Heyl et al.<sup>[35]</sup> For the transfer, polystyrene (PS, Sigma-Aldrich, average Mw ≈ 280 000) in toluene (Roth, ROTISOLV HPLC) (80 mg mL<sup>-1</sup>) was spin coated onto the exfoliated gold substrates (3500 rpm, 60 s), annealed for 10 min at 80 °C. Finally, the PS/MoS<sub>2</sub>/Au membrane was etched in KI/I<sub>2</sub> solution (Sigma-Aldrich, “Au etchant, standard”) to remove the Au layer. The final PS/MoS<sub>2</sub> was repeatedly washed in DI water to remove any residual etchant solution and transferred on the final substrate. The heterostructure photodetector was prepared by depositing the H<sub>2</sub>Pc (3 nm) layer *via* thermal evaporation method under vacuum ( $p = 10^{-7}$  mbar) upon ML of MoS<sub>2</sub>. The active layer structure is shown in Figure 1b.

**IPCE and IMPC Measurement:** To measure the incident-photon-to-current-efficiency (IPCE), light from a broadband light source (Philips Projection lamp Type 7724, 12 V, 100 W) was chopped and selected through a monochromator (Oriel Cornerstone 74 100) and pointed to the sample through a fiber and optical objective. The photocurrent signal preamplifier used a low-noise-current preamplifier (Stanford research system, ModelSR570) and extracted using a lock-in amplifier (EG&G Princeton Applied Research Model 5302). A 2400 source meter Keithley was used to apply 10 V bias across the cathodes (Au). For the steady state background illumination, samples were illuminated with a continuous-wave diode laser emitting at 620 nm. We realized that upon light exposure, the modulated current increased and saturated within the first 20 min, which may be caused by the desorption of oxygen from the MoS<sub>2</sub> surface or between ML-MoS<sub>2</sub> and sapphire. Therefore, for all the experiments described in the following, the devices were preilluminated for 30 min with steady-state light.

**Steady-State absorption:** An Agilent Cary-5000 UV-vis-NIR spectrometer was used to record the steady-state absorption spectra of samples over a range of 200–800 nm. The measurements were carried out in nitrogen environment.

## Supporting Information

Supporting Information is available from the Wiley Online Library or from the author.

## Acknowledgements

This work was funded by the German Science Foundation through the Collaborative Research Center HIOS (Projektnummer 182087777, SFB 951).

Open Access funding enabled and organized by Projekt DEAL.

## Conflict of Interest

The authors declare no conflict of interest.

## Data Availability Statement

The data that support the findings of this study are available from the corresponding author upon reasonable request.

## Keywords

hybrid organic/inorganic interfaces, intensity-modulated photocurrent spectroscopy, interfacial charge transfer, MoS<sub>2</sub>-based photodetectors response dynamics

Received: February 15, 2023

Revised: April 19, 2023

Published online: June 19, 2023

- [1] Z. Yu, Z. Y. Ong, S. Li, J. B. Xu, G. Zhang, Y. W. Zhang, Y. Shi, X. Wang, *Adv. Funct. Mater.* **2017**, *19*, 1604093.
- [2] O. Lopez-Sanchez, D. Lembke, M. Kayci, A. Radenovic, A. Kis, *Nat. Nanotechnol.* **2013**, *8*, 497.
- [3] Y. Xie, B. Zhang, S. Wang, D. Wang, A. Wang, Z. Wang, H. Yu, H. Zhang, Y. Chen, M. Zhao, B. Huang, L. Mei, J. Wang, *Adv. Mater.* **2017**, *29*, 1605972.
- [4] H. S. Nalwa, *RSC Adv.* **2020**, *10*, 30529.
- [5] A. Taffelli, S. Dirè, A. Quaranta, L. Panzeri, *Sensors* **2021**, *21*, 2758.
- [6] Q. Luo, G. Feng, Y. Song, E. Zhang, J. Yuan, D. Fa, W. Hu, *Nano Res.* **2022**, *15*, 8428.
- [7] A. George, M. V. Fistul, M. Gruenewald, D. Kaiser, T. Lehnert, R. Mupparapu, C. Neumann, U. Hübner, M. Schaal, N. Masurkar, L. M. R. Arava, I. Staude, U. Kaiser, T. Fritz, A. Turchanin, *npj 2D Mater. Appl.* **2021**, *5*, 15.
- [8] Chandan, S. Sarkar, B. Angadi, *Appl. Phys. Lett.* **2021**, *118*, 172105.
- [9] M. A. Muth, W. Mitchell, S. Tierney, T. A. Lada, X. Xue, H. Richter, M. Carrasco-Orozco, M. Thelakkat, *Nanotechnology* **2013**, *24*, 484001.
- [10] S. Berweger, H. Zhang, P. K. Sahoo, B. M. Kupp, J. L. Blackburn, E. M. Miller, T. M. Wallis, D. V. Voronine, P. Kabos, S. U. Nanayakkara, *ACS Nano* **2020**, *14*, 14080.
- [11] Y. C. Wu, C. H. Liu, S. Y. Chen, F. Y. Shih, P. H. Ho, C. W. Chen, C. te Liang, W. H. Wang, *Sci. Rep.* **2015**, *5*, 1.
- [12] K. Cho, T. Y. Kim, W. Park, J. Park, D. Kim, J. Jang, H. Jeong, S. Hong, T. Lee, *Nanotechnology* **2014**, *25*, 155201.
- [13] P. Han, E. R. Adler, Y. Liu, L. St Marie, A. El Fatimy, S. Melis, E. Van Keuren, P. Barbara, *Nanotechnology* **2019**, *30*, 284004.
- [14] J. K. Gustafson, D. Wines, E. Gulian, C. Ataca, L. M. Hayden, *J. Phys. Chem. C* **2021**, *125*, 8712.
- [15] D. Kufer, G. Konstantatos, *Nano Lett.* **2015**, *15*, 7307.
- [16] J. Jiang, C. Ling, T. Xu, W. Wang, X. Niu, A. Zafar, Z. Yan, X. Wang, Y. You, L. Sun, J. Lu, J. Wang, Z. Ni, *Adv. Mater.* **2018**, *30*, 1804332.
- [17] J. Pak, M. Min, K. Cho, D. H. Lien, G. H. Ahn, J. Jang, D. Yoo, S. Chung, A. Javey, T. Lee, *Appl. Phys. Lett.* **2016**, *109*, 183502.
- [18] J. Pak, J. Jang, K. Cho, T. Y. Kim, J. K. Kim, Y. Song, W. K. Hong, M. Min, H. Lee, T. Lee, *Nanoscale* **2015**, *7*, 18780.
- [19] Y. Huang, F. Zhuge, J. Hou, L. Lv, P. Luo, N. Zhou, L. Gan, T. Zhai, *ACS Nano* **2018**, *12*, 4062.
- [20] Z. Bielecki, K. Achtenberg, M. Kopytko, J. Mikołajczyk, J. Wojtas, A. Rogalski, *Bull. Bull. Pol. Acad. Sci. Tech. Sci.* **2022**, *70*, 1.
- [21] H. Fang, W. Hu, *Adv. Sci.* **2017**, *12*, 1700323.
- [22] N. Mutz, S. Park, T. Schultz, S. Sadofev, S. Dalgleish, L. Reissig, N. Koch, E. J. W. List-Kratochvil, S. Blumstengel, *J. Phys. Chem. C* **2020**, *124*, 2837.
- [23] S. H. Amsterdam, T. K. Stanev, L. Wang, Q. Zhou, S. Irgen-Gioro, S. Padgaonkar, A. A. Murthy, V. K. Sangwan, V. P. Dravid, E. A. Weiss, P. Darancet, M. K. Y. Chan, M. C. Hersam, N. P. Stern, T. J. Marks, *J. Am. Chem. Soc.* **2021**, *143*, 17153.
- [24] S. Padgaonkar, S. H. Amsterdam, H. Bergeron, K. Su, T. J. Marks, M. C. Hersam, E. A. Weiss, *J. Phys. Chem. C* **2019**, *123*, 13337.
- [25] T. R. Kafle, B. Kattel, P. Yao, P. Zereschki, H. Zhao, W. L. Chan, *J. Am. Chem. Soc.* **2019**, *141*, 11328.
- [26] M. M. Furchi, D. K. Polyushkin, A. Pospischil, T. Mueller, *Nano Lett.* **2014**, *14*, 6165.
- [27] A. Singh, A. K. Singh, *Phys. Rev. B* **2019**, *99*, 121201.
- [28] S. Zeiske, O. J. Sandberg, N. Zarrabi, W. Li, P. Meredith, A. Armin, *Nat. Commun.* **2021**, *12*, 3603.
- [29] O. Epshtein, G. Nakhmanovich, Y. Eichen, E. Ehrenfreund, *Phys. Rev. B* **2001**, *63*, 2.
- [30] A. Alegria, J. Colmenero, *Soft Matter* **2016**, *12*, 7709.
- [31] S. Najmaei, X. Zou, D. Er, J. Li, Z. Jin, W. Gao, Q. Zhang, S. Park, L. Ge, S. Lei, J. Kono, V. B. Shenoy, B. I. Yakobson, A. George, P. M. Ajayan, J. Lou, *Nano Lett.* **2014**, *14*, 1354.
- [32] D. Vaquero, V. Clerico, J. Salvador-Sanchez, E. Diaz, F. Dominguez-Adame, L. Chico, Y. M. Meziani, E. Diez, J. Quereda, *Nanoscale* **2021**, *13*, 16156.
- [33] J. H. Park, A. Sanne, Y. Guo, M. Amani, K. Zhang, H. C. P. Movva, J. A. Robinson, A. Javey, J. Robertson, S. K. Banerjee, A. C. Kummel, *Sci. Adv.* **2017**, *3*, e1701661.
- [34] S. Yim, S. Heutz, T. S. Jones, *J. Appl. Phys.* **2002**, *91*, 3632.
- [35] M. Heyl, D. Burmeister, T. Schultz, S. Pallasch, G. Ligorio, N. Koch, E. J. W. List-Kratochvil, *Phys. Status Solidi RRL* **2020**, *14*, 2000408.